

# The Continuing Slow Decline of AG Pegasi

Scott J. Kenyon

*Smithsonian Astrophysical Observatory, 60 Garden Street, Cambridge, MA 02138*

*skenyon@cfa.harvard.edu*

Daniel Proga

*NASA Goddard Space Flight Center, Laboratory for High Energy Astrophysics, Code 662,  
Greenbelt, MD 20771*

*proga@sobolev.gsfc.nasa.gov*

and

Charles D. Keyes

*Space Telescope Science Institute, 3700 San Martin Drive, Baltimore, MD 21218*

*keyes@stsci.edu*

*to be published in the*

**Astronomical Journal**

*July 2001*

## ABSTRACT

We analyze optical and ultraviolet observations of the symbiotic binary AG Pegasi acquired during 1992–97. The bolometric luminosity of the hot component declined by a factor of 2–3 from 1980–1985 to 1997. Since 1992, the effective temperature of the hot component may have declined by 10%–20%, but this decline is comparable to the measurement errors. Optical observations of  $H\beta$  and He I emission show a clear illumination effect, where high energy photons from the hot component ionize the outer atmosphere of the red giant. Simple illumination models generally account for the magnitude of the optical and ultraviolet emission line fluxes. High ionization emission lines – [Ne V], [Mg V], and [Fe VII] – suggest mechanical heating in the outer portions of the photoionized red giant wind. This emission probably originates in a low density region  $\sim 30$ –300 AU from the central binary.

*Subject headings:* stars: evolution – stars: novae – stars: individual (AG Pegasi)

## 1. INTRODUCTION

The symbiotic binary AG Peg began a slow nova eruption in the mid-1850’s, rising from 9th magnitude to 6th magnitude in  $\sim$  one decade or less (Lundmark 1921). Although spectra at optical maximum are not available, later spectra revealed a peculiar Be-type spectrum with strong P Cygni-like emission lines and additional absorption from He I and TiO (Fleming 1907; Payne-Gaposchkin 1957; Merrill 1916, 1929a,b, 1959). Since the 1920’s, the hot component of the binary has slowly evolved from a Be-type star to a Wolf-Rayet star (WN6 spectrum) to a hot “subdwarf” with an effective temperature exceeding  $10^5$  K (Gallagher et al. 1979; Kenyon et al. 1993, and references therein). The red giant companion to the eruptive star has an M3 spectral type, does not fill its tidal lobe, and loses mass in a low velocity wind (Kenyon & Fernández-Castro 1987; Kenny et al. 1991; Mürset & Schmid 1999).

The eruption of the hot component in AG Peg may be the slowest classical nova outburst ever recorded (Gallagher et al. 1979; Kenyon & Truran 1983; Nussbaumer 1992; Kenyon et al. 1993). Historical data – together with ultraviolet (UV) spectra acquired with the *International Ultraviolet Explorer* (*IUE*) and other UV satellite missions – indicate that the hot component maintained a roughly constant bolometric luminosity from  $\sim$  1850 to  $\sim$  1980. The last few pairs of *IUE* spectra suggest that the luminosity of the hot component began to decline as the intensity of the broad emission lines weakened considerably (Kenyon et al. 1993; Vogel & Nussbaumer 1994, Nussbaumer, Schmutz, & Vogel 1995). At about the same time, the source of strong emission lines may have shifted from an H II region surrounding the hot component to the illuminated hemisphere of the red giant (e.g., Proga, Kenyon, & Raymond 1998). Radio, X-ray, and other satellite data show features indicative of colliding winds, where material ejected from the hot component interacts with the slow-moving wind of the red giant (Kenny et al. 1991; Mürset et al. 1995; Nussbaumer et al. 1995; Contini 1997). If these analyses are correct, the hot component may be slowly transforming from a slow classical nova at maximum into a nova remnant.

To elucidate further the slow decline of the hot component in AG Peg, we analyzed new optical spectra and UV spectra acquired with the *Hubble Space Telescope* (*HST*). The optical spectra demonstrate that most of the low ionization emission lines, such as H I and He I, arise in the photoionized wind of the red giant. Some high ionization emission from He II is also produced in this region. Although more spectra are required to follow the evolution of the hot component in detail, the UV data provide further evidence for a decline in the bolometric luminosity of the hot component. The forbidden and intercombination emission lines indicate that an ionized nebula with a wide range of densities,  $\sim 10^5$  to  $10^{10}$  cm $^{-3}$ , surrounds the binary system. Lines of low ionization potential, e.g., [O III], suggest a low density, photoionized nebula with an electron temperature,  $T_e \sim 10^4$  K; lines of higher ionization potential, e.g., [Ne V] and [Fe VII], are formed at higher electron density,  $n_e \sim 10^7$  cm $^{-3}$ , in gas mechanically heated to electron temperatures of at least  $10^5$  K.

We describe the *HST* and new optical data in §2, analyze these data in §3, and conclude with

a brief summary in §4.

## 2. OBSERVATIONS

We acquired high quality ultraviolet and optical spectra of AG Peg with the *Faint Object Spectrograph* (FOS) on board the *Hubble Space Telescope*. These data were taken as part of a calibration program to evaluate the absolute FOS wavelength scale and to measure the throughput for the small apertures and the amount of internal “out of band” grating scatter recorded in FOS exposures. The spectra cover 1150–4800 Å at a resolution of  $R = 1300$  over the entire spectrum. To attain the best photometric accuracy, the most precise target acquisition and centering procedure was used. The centering accuracy should be roughly  $0''.025$  for all of the data, with a  $1\sigma$  uncertainty in the HST guiding and orbit-to-orbit re-centering of  $0''.007$ . Most of the observations were taken in RAPID mode, which yields several individual readouts of the spectrum. We averaged all readouts to produce a final spectrum for each wavelength region. We acquired observations with both FOS detectors, FOS/BL and FOS/RD, through several apertures,  $4''.3$  square,  $1''.0$  round,  $0''.5$  round, and  $0''.3$  round. Observations with the largest apertures should have the best photometric accuracy. In practice, line fluxes derived from different apertures agreed to 5% or better; we thus averaged the line and continuum fluxes described below.

We reduced the data using the standard “calfos” pipeline routines in STSDAS using the STScI-recommended reference files and calibration procedures appropriate to each epoch of observation. Thus, the FOS calibration closeout reference file suite, as described in the HST Data Handbook, Volume II (Keyes 1997), was used for all data.

P. Berlind, D. Koranyi, and T. Lappin acquired low resolution optical spectra of AG Peg with the FAST spectrograph mounted at the Fred L. Whipple Observatory 1.5-m telescope on Mount Hopkins, Arizona. FAST is a high throughput, slit spectrograph equipped with a thinned, back-side illuminated  $320 \times 2704$  Loral CCD (Fabricant et al. 1998). These spectra cover 3800–7500 Å at a resolution of  $\sim 3$  Å with a  $3''$  slit. We calibrated the FAST spectra on the Hayes & Latham (1975) flux scale using observations of standards from Barnes & Hayes (1982). Repeat observations of several standards and a comparison of photoelectric B and V magnitudes with those derived from the spectra indicate the calibration has an uncertainty of  $\pm 0.10$  mag.

We acquired additional optical spectrophotometry of AG Peg on 1992 November 5–11 with the white spectrograph and GoldCam CCD dewar (WhiteCam) at the Kitt Peak National Observatory (KPNO) 0.9-m telescope. Grating 26 and a  $7''.5$  slit resulted in a resolution of  $\sim 10$  Å on a Ford  $3K \times 1K$  CCD. Roughly 200–300 pixels at each end of the CCD are vignetted with WhiteCam, which reduced our free spectral range to 3500–6200 Å at  $1.25$  Å/pixel. This interval includes most of the strong emission lines detected on the FAST spectra but misses  $H\alpha$  and several He I lines. We reduced these data to the Hayes & Latham (1975) flux scale using observations of standard stars from Barnes & Hayes (1982) and estimate our flux calibration has an uncertainty of  $\pm 0.05$

mag.

Figure 1 shows a composite *FOS* spectrum. The data shown in this figure and all subsequent figures have not been corrected for interstellar extinction. The spectrum has a Rayleigh-Jeans tail from a hot continuum for  $\lambda \lesssim 2000$  Å, a flat nebular continuum for  $\lambda \approx 2000$ –3646 Å, and a red continuum from the cool giant for  $\lambda \gtrsim 4000$  Å. Strong emission lines from a wide range of ionization states are superimposed on these continua. FAST spectra show a red continuum, strong TiO absorption bands, and more emission lines at longer wavelengths (see Figure 1 of Kenyon et al. 1993). The overall appearance of the spectrum has changed slightly since the early 1990’s: the Rayleigh-Jeans tail and the nebular continuum are more prominent on the *FOS* spectra than on earlier *IUE* spectra.

To quantify the spectral changes of AG Peg, we measured continuum magnitudes and emission line fluxes on all of the spectra. We define narrow-band continuum magnitudes in 30 Å bandpasses as

$$m_{\lambda} = -2.5 \log F_{\lambda} - 21.1 , \quad (1)$$

where  $F_{\lambda}$  is the average flux in the bandpass. Tables 1 and 2 list continuum magnitudes and  $1\sigma$  errors derived from the *FOS* and the FAST/WhiteCam observations. We measured emission line fluxes using interactive gaussian fitting routines. Simple gaussians produce good fits for all emission lines except H $\alpha$ , which has a broad wing superimposed on a narrow gaussian feature. We used two gaussians to fit this feature. Tables 3–5 list emission line fluxes for the *FOS* and the FAST/WhiteCam observations. The typical error for FAST measurements in Table 5 is 5% for strong lines and 10% for weak lines based on repeat FAST observations acquired on the same night and a comparison of contemporaneous FAST and *FOS* observations. The *FOS* line fluxes in Tables 3–4 have accuracies of 5% or better.

Figure 2 shows the continuing slow decline of the far ultraviolet (far-UV) and near-ultraviolet (near-UV) continuum. We adopt the Fernie (1985) photometric ephemeris to time maximum light in the system, when the hot component lies in front of the red giant:

$$\text{Max(V)} = \text{JD } 2442710.1 + 816.5 \cdot E. \quad (2)$$

Data in Figure 2 and subsequent figures for photometric phases less than 7 are from Keyes (1981) and Kenyon et al. (1993). In addition to the 2.0–2.5 mag decline at 1300–3300 Å, there are obvious maxima in the near-UV continuum at  $\phi = 2, 7$ , and 8. These maxima have amplitudes of 0.5–1.0 mag and are weak or absent in the far-UV.

Figures 3 and 4 show that several emission lines vary in step with the near-UV continuum. The N IV]  $\lambda 1486$  line rises by a factor of two at  $\phi = 2$  and has a weaker rise at  $\phi = 8$ . He II  $\lambda 1640$  displays the opposite behavior, with a weak rise at  $\phi = 2$  followed by a stronger variation at  $\phi = 8$ .

Both lines were saturated on *IUE* spectra at  $\phi = 7$ . The optical lines shown in Figure 4 have more obvious variations correlated with photometric phase. The H I and He I lines are roughly a factor of two more intense at  $\phi = 8$  and  $\phi = 9$  than at photometric minima. Higher ionization optical lines, such as He II  $\lambda 4686$ , have a weak maximum. Both sets of lines are a factor of 2–3 weaker at  $\phi = 8$ –9 compared to data at  $\phi = 2$ –4.

### 3. ANALYSIS

The behavior of the lines and continuum in AG Peg continue to support the phenomenological model developed by Belyakina (1968a, b, 1970), Boyarchuk (1966, 1967), and Gallagher et al. (1979). The overall decrease in the optical and UV line and continuum fluxes results from the continuing slow nova-like decline of the hot component. Kenyon et al. (1993) showed that the bolometric luminosity of the hot component has remained roughly constant for nearly a century (see also Gallagher et al. 1979). As the photospheric radius contracted, the effective temperature of the hot component increased. The optical and UV continua faded. Fluxes from low ionization lines also declined; fluxes from the highest ionization lines increased. Because high energy photons from the hot component ionize the outer atmosphere of the red giant, the system displays photometric maxima in phase with the orbit. The nebular continuum and recombination lines of H I and He I are strongest when we see the heated hemisphere and weakest when we see the opposite, unheated hemisphere. Prior to 1990, higher ionization lines formed closer to the hot component; the fluxes of these lines thus were only weakly modulated by the orbit.

The high quality *FOS* and *FAST* data yield new tests of this picture. Based on an analysis of *IUE* data, Kenyon et al. (1993) suggested that AG Peg might be evolving towards lower luminosities along a white dwarf cooling curve. They proposed that the transition from a Wolf-Rayet spectrum with broad emission lines to a nebular spectrum with narrow emission lines marked the start of this evolution. At the same time, the source of the strong high ionization emission lines moved from an H II region surrounding the hot component to the illuminated hemisphere of the red giant. Contini (1997) and several other studies suggest that some emission features form in an interaction region between the two stars, where the low velocity wind of the red giant collides with the higher velocity wind from the hot component.

To test these proposals in more detail, we first consider the evolution of the hot component in §3.1. We then analyze emission lines produced in the illuminated red giant atmosphere (§3.2) and in shocked gas in the outer portions of the red giant wind (§3.3). We conclude this section with some comments on colliding winds in the AG Peg binary (§3.4).

### 3.1. Evolution of the Hot Component

To understand the evolution of the hot component, we follow previous studies and derive the time variation of luminosity  $L_h$  and effective temperature  $T_h$ . Because the complete energy distribution of the hot component cannot be observed directly, we need accurate proxies for  $L_h$  and  $T_h$ . Three techniques have been proposed in previous studies. Kenyon & Webbink (1984) adopted a blackbody model for the hot component and predicted UV color indices for sources surrounded by a photoionized nebula; Kenyon (1985) generalized this approach and derived  $L_h$  and  $T_h$  from fits to the UV spectral energy distribution (see also Kenyon et al. 1993). Fernández-Castro et al. (1988) developed a UV Zanstra temperature to derive  $T_h$  from measurements of the He II  $\lambda 1640$  emission line and the continuum flux at 1400 Å. Mürset et al. (1991; see also Keyes 1981; Mürset & Nussbaumer 1994) estimated  $L_h$  and  $T_h$  from He II  $\lambda 1640$  and the UV spectral energy distribution. Following Iijima (1981), Kenyon (1986) inferred  $L_h$  and  $T_h$  from the optical H I and He II lines, which are less sensitive to uncertainties in the interstellar extinction to the source.

Figure 5 shows results for the time variation of  $L_h$  and  $T_h$  in AG Peg from these three techniques. We used data from Keyes (1981), Kenyon et al. (1993), and this paper, corrected for  $E_{B-V} = 0.10$  using the Mathis (1990) extinction curve for an adopted distance of 800 pc. We estimate  $L_h$  and  $T_h$  from (i) the UV continuum fits of Kenyon (1985), (ii) the UV Zanstra temperature of Fernández-Castro et al. (1988), and (iii) the optical Zanstra temperature of Kenyon (1986). The formal uncertainties are  $\pm 0.1$  in  $\log L_h$  and  $\pm 0.05$  in  $\log T_h$ . The uncertain distance adds a systematic uncertainty to the luminosity but not to the effective temperature. In the top panel, the luminosity derived from the UV Zanstra temperature monotonically decreases from  $\phi = 1$  to  $\phi = 9$  (filled circles). The luminosity derived from the UV continuum is roughly constant with time and may decline some at  $\phi \geq 7-8$  (plus signs). As expected, the luminosity derived from optical data follows the illumination effect (open circles):  $L_h$  is largest at photometric maxima and smallest at photometric minima. The average luminosity is comparable to the  $L_h$  derived from UV data and shows the same overall trend: a roughly constant  $L_h$  for  $\phi = 1-7$  followed by a decline.

The time evolution of  $T_h$  is shown in the lower panel of Figure 5. The  $T_h$  derived from the optical emission lines is always 25% to 50% larger than the  $T_h$  estimated from the UV lines. This difference is easily understood. Because the H I line fluxes change by factors of 2–3 with orbital phase, the flux ratio  $F(\lambda 4686)/F(\lambda 4861)$  is largest at photometric minima and smallest at photometric maxima. The  $T_h$  derived from this ratio thus varies with phase, as shown by the open circles in Figure 5. The  $L_h$  derived from the optical line fluxes is anti-correlated with  $T_h$ . For much of the evolution, the  $T_h$  derived from the UV continuum is 25% to 50% smaller than the  $T_h$  estimated from the UV lines (plus signs). AG Peg resembled a Wolf-Rayet star during this period; its UV energy distribution was very similar to the energy distribution of the luminous Wolf-Rayet star HD 50896. Assuming that the Hillier (1987) models for HD 50896 also fit AG Peg, Kenyon et al. (1993) derived a luminosity for the hot component in AG Peg from the observed *Voyager* spectrum. This estimate is  $\sim 50\%$  larger than derived from UV continuum fits. To produce a larger luminosity from the same continuum flux, the  $T_h$  implied by this analysis must also be  $\sim$

50% larger. Broad Wolf-Rayet emission lines began to disappear from low resolution UV spectra of AG Peg at  $\phi \geq 6$ . The UV continuum data then begin to yield a  $T_h$  similar to that derived from the UV Zanstra temperature.

This analysis suggests that the results for  $L_h$  and  $T_h$  from the UV Zanstra temperature are more reliable indicators of the evolution of the hot component in AG Peg. We conclude that  $L_h$  was roughly constant during  $\phi = 1$ –3, when  $T_h$  rose by  $\sim 20\%$ . As  $T_h$  remained roughly constant at  $\phi = 3$ –8,  $L_h$  declined by a factor of 2–3. The *HST* data suggest that  $T_h$  may have declined by  $\sim 10\%$  to  $20\%$  during  $\phi = 8.0$ –9.5, but this decline is comparable to the size of the uncertainties in the temperature estimates.

### 3.2. Illumination of the Red Giant

Since the 1930’s, the ionization of the red giant atmosphere by the hot component has been an important feature of the AG Peg binary (see Merrill 1959; Belyakina 1970, and references therein). Merrill’s observations demonstrated that fluxes of low ionization emission lines vary in phase with the orbital motion of the red giant. Belyakina (1970) interpreted these variations as the reflection effect, where the hot component heats the outer red giant atmosphere. She showed that the observed amplitude and the relative phasing of the variation were consistent with model predictions. The observed variations in He II and other high ionization lines, however, were not consistent with the reflection effect. The radial velocity variations and the broad widths –  $\sim 1000$  km s $^{-1}$  – of these features were more consistent with line formation in the outer atmosphere of the hot component.

Evolution of the emission line fluxes in 1985–1990 suggest a modest change in this picture. The broad WN-type emission lines from He II, N V, and other species faded to reveal narrow emission features with profiles similar to those of low ionization lines (Kenyon et al. 1993). Although the phase coverage of the UV data is poor after  $\sim 1990$ , our optical data show a weak modulation of He II with orbital phase (Figure 4). This behavior suggests that at least some He II emission is produced in the ionized red giant atmosphere.

To investigate the illumination of the red giant atmosphere in more detail, Proga et al. (1996, 1998) developed a non-LTE photoionization model. They showed that the spectrum of an illuminated red giant atmosphere is too weak to explain the strong line spectrum observed in AG Peg and other symbiotic stars. A normal red giant does not intercept enough radiation from the hot component to produce prominent emission lines (Proga et al. 1996). However, a red giant wind can intercept enough high energy photons from the hot component if the optical depth in the wind is large (Proga et al. 1998). Winds with mass loss rates of  $10^{-7}$  M $_{\odot}$  yr $^{-1}$  can generally account for the observations of symbiotics such as AG Peg. These models reproduce observed fluxes of metallic lines if the O/N and C/N abundances are similar to those of field red giants. Predicted fluxes for H and He lines fall below the observations.

Proga et al. (1998) summarized the simplifications and weaknesses of their calculations. They derived an accurate solution for illumination along the line of centers connecting the two stars and assumed that the total flux from the illuminated atmosphere  $F_{tot}$  is

$$F_{tot} = r_{cs} F_{1D} , \quad (3)$$

where  $F_{1D}$  is the flux derived from a unit area along the line of centers and  $r_{cs}$  is the geometric cross-section of the red giant wind. This simplification ignores any wind from the hot component, the complex geometry of the red giant wind, and any interaction region between the two winds. Proga et al. noted that this simplified approach was a first step in understanding complex systems like AG Peg and many other symbiotics. They suggested several ways to reconcile the model with the observations and commented that better observations of weaker UV and optical lines might allow a choice between different models.

As a further guide to understanding illumination in AG Peg, we compare our new data with the theoretical results of Proga et al. (1996, 1998). Figure 6 indicates line fluxes for wind models and observations of AG Peg (the lines are  $H\beta$ , He I  $\lambda 5876$ , O III]  $\lambda 1664$ , CIV  $\lambda 1550$ , He II  $\lambda 4686$ , and N V  $\lambda 1240$ ). We use the data from this paper (filled triangles,  $\phi \approx 9$ ) and from Kenyon et al. (1993, open circles,  $\phi \approx 7-8$ ). The solid and dashed lines indicate model predictions of Proga et al. (1996, 1998). We adopt  $T_h = 10^5$  K and  $L_h = 620 L_\odot$  for the hot component, and use red giant parameters for Vogel’s velocity law (Vogel 1991) with red giant mass loss rates of  $\dot{M} = 10^{-8}$  and  $10^{-6} M_\odot \text{ yr}^{-1}$  (see also Figure 12 in Proga et al. 1998). Solid curves show predictions for  $r_{cs} = R_g^2$ ; dashed curves show predictions for  $r_{cs} = 3^2 R_g^2$ . The line fluxes increase with  $\dot{M}$  for each set of models. Because the emission measure of the ionized wind increases linearly with  $\dot{M}$ , the predicted line fluxes vary approximately linearly with  $\dot{M}$  at high  $\dot{M}$ . At lower mass loss rates, the line fluxes are limited by the amount of material in the *static* red giant atmosphere. This material provides a lower limit to the emission measure – for a particular hot component luminosity – so the line fluxes vary little for  $\dot{M} \lesssim 10^{-8} M_\odot \text{ yr}^{-1}$ .

Figure 6 shows that the fluxes of all emission lines decreased by a factor of 1.5–3.0 during  $\phi = 7-9.5$ . This decline in the fluxes coincides with the appearance of a modest orbital modulation of the He II line fluxes (see Figures 3–4). We interpret this behavior as a change in the location of high ionization emission lines. Prior to  $\phi = 7$ , nearly all of the high ionization lines formed in a compact H II region surrounding the hot component (see Figure 11 of Kenyon et al. 1993). These lines were broad and diffuse, as expected for material in an outflowing wind from a hot, luminous white dwarf star. After  $\phi = 7$ , the lines are narrow; the illuminated red giant atmosphere produces some of the high ionization line emission. Thus, the illumination model can better account for observations at  $\phi \approx 9$  than at  $\phi \approx 7$ . Observed fluxes at  $\phi = 7$  lie above optimistic model predictions (dashed lines); data for  $\phi = 9$  generally lie below these predictions. Although the illumination models are still crude, it is encouraging that as the wind from the hot component weakens and AG Peg becomes a less complex system, the models can better explain the observations

with reasonable input parameters.

### 3.3. High Ionization Forbidden Lines

The ionized nebula surrounding AG Peg consists of several distinct components. The 1–20 cm VLA data are consistent with an unresolved central source embedded in several extended shells of gas (Kenny et al. 1991; Seaquist & Taylor 1992; Taylor & Seaquist 1984). The unresolved radio source is probably optically thick, free-free emission from the photoionized wind of the red giant (Kenny et al. 1991; Seaquist & Taylor 1992; Kenyon et al. 1993). Kenyon et al. (1993) suggested that most of the [O III] and [Ne III] emission observed in 1980–93 is also produced in this volume (see also Kenny et al. 1991). These lines have continued to decline in intensity since 1993; their flux ratios are consistent with an electron density,  $n_e \lesssim 10^7 \text{ cm}^{-3}$ , for an electron temperature,  $T_e \sim 10^4 \text{ K}$  (Ferland & Shields 1978). This evolution suggests an overall decrease in the electron density during the past decade.

Kenyon et al. (1993) noted that results for high ionization forbidden lines were uncertain because the lines were not very prominent on their relatively low signal-to-noise spectra. The new FAST and *HST* data allow us to make more progress on this region. We have accurate UV and optical fluxes for several [Fe VII], [Mg V], and [Ne V] lines, which yield more information on the ionized nebula.

We begin with the [Fe VII] lines, which have remained roughly constant in intensity since their first appearance in 1984–1986. Several [Fe VII] intensity ratios,  $I(\lambda 5721)/I(\lambda 6087)$  and  $I(\lambda 3586)/I(\lambda 3758)$ , do not depend on  $n_e$  or  $T_e$ . Our result for  $I(\lambda 5721)/I(\lambda 6087)$ , 0.6–0.8, brackets the predicted value of 0.65; our result for  $I(\lambda 3586)/I(\lambda 3758)$ , 0.3, is significantly smaller than the predicted value of 0.75. The small observed value of the  $I(\lambda 3586)/I(\lambda 3758)$  ratio suggests that the  $\lambda 3758$  line is blended with an O III Bowen fluorescence line. The relative intensities of other O III lines suggest that O III  $\lambda 3758$  should contribute  $\sim 2/3$  to  $3/4$  of the  $\lambda 3758$  flux. If so, the [Fe VII]  $I(\lambda 3586)/I(\lambda 3758)$  ratio is then close to the predicted value (see Tables 3–4 and Saraph & Seaton 1980).

With this correction to the  $I(\lambda 3758)$  flux, the reddening-corrected [Fe VII] intensity ratios sensitive to density and temperature are  $I(\lambda 2015)/I(\lambda 3758) \approx 0.4\text{--}0.6$  and  $I(\lambda 3758)/I(\lambda 6087) \approx 1.1\text{--}1.4$ . Both intensity ratios are consistent with  $T_e \lesssim 3 \times 10^4 \text{ K}$  if  $n_e \gtrsim 10^8 \text{ cm}^{-3}$  and  $T_e \gtrsim 5 \times 10^4 \text{ K}$  if  $n_e \lesssim 10^8 \text{ cm}^{-3}$  (Nussbaumer & Storey 1982; Keenan & Norrington 1987, 1991). Weak detections of [Fe VII]  $\lambda\lambda 4942, 5159$  favor  $n_e \sim 10^7 \text{ cm}^{-3}$  over other values.

To better constrain the physical conditions in the  $\text{Fe}^{+6}$  region, we also consider data for [Ne V]. The ionization potential of  $\text{Ne}^{+4}$  (126 eV) is comparable to  $\text{Fe}^{+6}$  (128 eV); [Ne V] and [Fe VII] should form in similar physical conditions. The intensity ratio for  $I(\lambda 3346)/I(\lambda 3426)$  is 0.3–0.5, which brackets the predicted value of 0.36 (Nussbaumer & Rusca 1979). The  $I(\lambda 3426)/I(\lambda 2976)$  intensity ratio is sensitive to  $n_e$  and  $T_e$  (Kafatos & Lynch 1980). Our measured ratio of  $I(\lambda 3426)/I(\lambda 2976)$

$\approx 17$  requires  $n_e \lesssim 10^7 \text{ cm}^{-3}$  for  $T_e \gtrsim 10^5 \text{ K}$ .

The critical densities for all of the [Fe VII] and [Ne V] lines on our spectra are  $10^7 \text{ cm}^{-3}$  to  $10^8 \text{ cm}^{-3}$  (Kafatos & Lynch 1980; Nussbaumer & Storey 1982; Keenan & Norrington 1987, 1991). Although there are some uncertainties in the atomic physics for both ions, the line ratios strongly imply line formation in a very hot, low density gas. This result favors mechanical heating over photoionization as the energy source for this emission. To place a better limit on the electron density and on the origin of the highly ionized forbidden lines, we can estimate the forbidden line fluxes expected from a photoionized gas. The volume  $V$  for the [Fe VII] Strömgren sphere is

$$V = N_\gamma / n_{Fe} n_e \alpha_r, \quad (4)$$

where  $N_\gamma$  is the number of  $Fe^{+5}$ -ionizing photons,  $n_{Fe}$  is the number density of Fe atoms, and  $\alpha_r$  is the recombination rate. The luminosity in a single [Fe VII] emission line is

$$L_{[Fe \text{ VII}]} = x_i n_{Fe+6} A_{ji} h\nu_{ij} V, \quad (5)$$

where  $x_i$  is the fraction of Fe VII ions in the  $j$ th level,  $n_{Fe+6}$  is the number density of Fe VII ions,  $A_{ji}$  is the transition probability, and  $\nu_{ij}$  is the line frequency. If we assume that all of the Fe in the nebula is in the form of Fe VII, substitute our expression for the volume into equation (5) and adopt the appropriate coefficients (Woods, Shull, & Sarazin 1981; Nussbaumer & Storey 1982; Keenan & Norrington 1987; Arnaud & Raymond 1992), the luminosity in the  $\lambda 6087$  line is

$$L_{\lambda 6087} \approx 0.1 L_\odot \left( \frac{N_\gamma}{10^{43} \text{ s}^{-1}} \right) \left( \frac{10^8 \text{ cm}^{-3}}{n_e} \right). \quad (6)$$

The coefficient in equation (6) varies by a factor of 2–3 for  $T_e = 10^4 \text{ K}$  to  $10^5 \text{ K}$  if the hot component has an effective temperature of  $10^5 \text{ K}$  and emits as a blackbody. This result – together with similar expressions for other [Fe VII] and [Ne V] lines – suggests that photoionization can account for the observed optical and ultraviolet line fluxes,  $L_{obs} \sim 0.05\text{--}0.10 L_\odot$ , for  $n_e \lesssim 10^8 \text{ cm}^{-3}$ . Although photoionization rarely produces the large electron temperatures,  $T_e \sim 10^5 \text{ K}$ , implied by the intensity ratios of the forbidden lines, this limit on the electron density is consistent with the electron density derived from the flux ratios of the [Ne V] and [Fe VII] lines,  $n_e \lesssim 10^7 \text{ cm}^{-3}$ .

We conclude that the [Fe VII] and [Ne V] emission comes from a region with a low electron density,  $n_e \lesssim 10^7 \text{ cm}^{-3}$ , and a relatively high electron temperature  $T_e > 10^5 \text{ K}$ . These regions have considerable emission measures,  $n_e^2 V \sim 10^{57} \text{ cm}^{-3}$ , for  $T_e \sim 10^5 \text{ K}$  and  $n_e \sim 10^7 \text{ cm}^{-3}$ . The size of the spherical  $Ne^{+4}$ – $Fe^{+6}$  zone is  $\sim 10 \text{ AU}$ . Although the hot component emits enough high energy photons to produce large [Ne V] and [Fe VII] emission regions, the large electron temperature indicates that mechanical heating also is an important energy source. If the high ionization gas forms in a thin shell with a thickness of  $\lesssim 1 \text{ AU}$ , the shell lies  $\gtrsim 30 \text{ AU}$  from the central binary.

The [Mg V] features are the last set of useful high ionization forbidden lines in AG Peg. The ionization potential of  $Mg^{+4}$  (141 eV) is larger than for  $Ne^{+4}$  and  $Fe^{+6}$ . The critical density for

both  $\lambda 2784$  and  $\lambda 2930$  is  $n_e = 10^8 \text{ cm}^{-3}$ . The intensity ratio,  $I(\lambda 2784)/I(\lambda 2930) = 3.4$ , is very close to the predicted value of 3.7 (Kafatos & Lynch 1980). The  $I(\lambda 2784)/I(\lambda 2417)$  intensity ratio is sensitive to  $n_e$  and  $T_e$  (Kafatos & Lynch 1980). Our measured ratio of  $I(\lambda 2784)/I(\lambda 2417) = 10$  requires  $n_e \lesssim 10^9 \text{ cm}^{-3}$  for  $T_e > 10^5 \text{ K}$ . This density is close to the critical density for  $\lambda 2417$ . Thus, this emission forms in denser material than the [Ne V] and [Fe VII] lines. The emission measure for [Mg V] suggests a shell which is factor of 10 or more thinner than the  $\text{Ne}^{+4}$ – $\text{Fe}^{+6}$  zone.

### 3.4. Colliding Winds and Shocks

Colliding winds have become a popular explanation for high energy phenomena in symbiotic and other interacting binary systems (e.g., Wallerstein & Brugel 1988; Nussbaumer & Walder 1993; Mürset et al. 1995; Formigini, Contini & Leibowitz 1995; Contini 1997; Contini & Formigini 1999). First developed by Kwok & Leahy (1984) and Wallerstein et al. (1984, see also Willson et al. 1984), these models use the kinetic energy in the winds from the red giant and the hot component – instead of photoionization – to power X-rays and high ionization emission lines observed in many systems (Girard & Willson 1987; Nussbaumer & Vogel 1989). The momenta in the two winds roughly balance in an interaction region, where shocks produce X-ray emission and lead to the formation of highly ionized atomic species. The bow-shape of the interaction region also naturally produces emission line profiles similar to those observed in some systems.

The intensity ratios of the high ionization forbidden lines in AG Peg suggest that some of the ionized nebula in this system is mechanically heated (see also Contini 1997). For the hot component effective temperatures and bolometric luminosities observed in most symbiotic stars, photoionization yields much smaller electron temperatures,  $\sim 1\text{--}3 \times 10^4 \text{ K}$ , for  $n_e \sim 10^5$  to  $10^{10} \text{ cm}^{-3}$  (e.g., Mürset & Nussbaumer 1994; Schwank et al. 1997; Proga et al. 1996, 1998). We showed in §3.3 that photoionization can explain the observed line fluxes for  $n_e \lesssim 10^8 \text{ cm}^{-3}$ . Shocks from colliding winds are a natural mechanism to produce high temperature gas. We now consider whether colliding winds in the system can also power the line fluxes.

Two sources of mechanical energy can potentially power the forbidden line emission in AG Peg: (i) an interaction region between the two stars, where material recently lost by the hot component collides with matter recently ejected by the red giant (see Contini 1997; Nussbaumer & Walder 1993), or (ii) the ‘inner nebula’ of Kenny et al. (1991), where material ejected throughout the outburst compresses gas lost by the red giant prior to the outburst.

The outer atmosphere of the red giant is a promising source of mechanically heated gas in AG Peg (see Contini 1997, and references therein). This region has the required density and emission measure. From Figure 1a of Proga et al. (1998), the density in the red giant wind is  $n_e \sim 10^7 \text{ cm}^{-3}$  at distances of  $\sim 10 \text{ AU}$  from the central binary. The density falls to  $n_e \sim 3 \times 10^6 \text{ cm}^{-3}$  at  $\sim 30 \text{ AU}$ . The shock velocity needed to reach electron temperatures exceeding  $10^5 \text{ K}$  is modest,  $\sim 10\text{--}20 \text{ km s}^{-1}$ , compared to the red giant wind velocity of  $30\text{--}60 \text{ km s}^{-1}$  (Kenny et al. 1991).

As envisioned in the Wallerstein et al. (1984) picture, the colliding winds of the red giant and the hot component might yield this shock velocity if the collision is oblique. Achieving the proper forbidden line energy from this region, however, may be difficult. For a shock velocity of  $10\text{--}20\text{ km s}^{-1}$ , the mechanical energy in the wind is  $\sim 0.001\text{--}0.004\text{ L}_\odot$  for a red giant mass loss rate of  $\sim 10^{-7}\text{ M}_\odot\text{ yr}^{-1}$ . This energy is small compared to the luminosity in a single [Ne V] forbidden line,  $\sim 0.05\text{--}0.10\text{ L}_\odot$ . Much larger mass loss rates are ruled out by the radio data; much larger shock velocities imply higher ionization emission lines such as [Fe X] not detected on our spectra. The wind from the hot component does not help this problem significantly: the mass loss rate is now probably smaller than that of the giant (Kenyon et al. 1993; Nussbaumer et al. 1995) and the wind velocity of  $1000\text{ km s}^{-1}$  is much larger than the needed shock velocity unless we have considerably underestimated the electron temperature of the forbidden line region.

The inner radio nebula of Kenny et al. (1991) is also a potential location for shocked gas in AG Peg. The compressed inner shell of this nebula is an ideal location for shocks. The apparent gas velocity of  $\sim 60\text{ km s}^{-1}$  is close to the  $10\text{--}20\text{ km s}^{-1}$  shock velocity required for  $10^5\text{ K}$  gas. The emission measure of this material,  $n_e^2 V \sim 10^{57}\text{ cm}^{-3}$  (Kenny et al. 1991), is identical to our estimate for the  $\text{Ne}^{+4}\text{--Fe}^{+6}$  zone. However, there is an important problem associating the high ionization forbidden lines with this region. From fits to the radio spectral index and flux from the inner nebula, Kenny et al. (1991) estimate  $n_e \approx 2 \times 10^4\text{ cm}^{-3}$  for the compressed shell. This density is a factor of  $\sim 10^3$  smaller than our estimate from the [Ne V] and [Fe VII] line ratios. The luminosity of the compressed shell is also insufficient to power the forbidden lines. Kenny et al. (1991) derive a rate  $3 \pm 3 \times 10^{-6}\text{ M}_\odot\text{ yr}^{-1}$  for spherical mass loss, which implies a mechanical luminosity of  $\sim 0.2\text{ L}_\odot$  for a  $20\text{ km s}^{-1}$  shock. The observed luminosity in the [Ne V] and [Fe VII] lines exceeds this estimate by a factor of  $\sim 2$ .

Both explanations for shocked gas in the AG Peg wind are sensitive to the adopted distance. For a given radio flux, the mass loss rate is linearly proportional to the distance. The optical emission line luminosity depends on the square of the distance. Better agreement between observations and theory requires a smaller distance than our adopted value of  $800\text{ pc}$ . Either of our explanations for the shocked gas requires a distance of  $400\text{ pc}$  or less to allow the mechanical energy in the wind to match the energy needed for the high ionization forbidden lines. Such a small distance seems ruled out by Kenny et al. (1991), who prefer a  $600\text{ pc}$  distance to reconcile the size of the inner nebula with proper motion data.

We thus conclude that neither colliding wind picture for the formation of high ionization forbidden lines can account for the observed line fluxes in AG Peg. If the hot component emits enough high energy photons to account for the forbidden line fluxes, mechanical heating from the colliding winds may explain the high electron temperatures. A detailed photoionization calculation which includes shock excitation would test this proposal.

Making more progress on the high ionization forbidden lines also requires new observations to constrain the geometry of the ionized nebula. At a distance of more than  $0''.5$  from the central

binary, the inner nebula of Kenny et al. (1991) can be resolved with STIS on board *HST*. These observations would test the notion that the forbidden emission lines form well outside the red giant atmosphere. Resolving the nebula at 30 AU,  $\sim 0''.05$  from the central binary, is more difficult but may be possible with ground-based interferometers or future space missions. Higher spectral resolution UV or optical observations would yield line profiles for the high ionization lines and provide better constraints on the shock velocity and geometry.

#### 4. Summary

Our analysis of new optical and UV data demonstrates that the AG Peg binary continues to evolve. The optical data show clear evidence for a more pronounced reflection effect, where high energy photons from the hot component ionize the wind and outer atmosphere of the red giant (Boyarchuk 1966; Belyakina 1970; Kenyon & Gallagher 1983). Many low ionization optical lines, such as H I and He I form in this region. Some high ionization optical emission lines, such as He II, also form in the ionized wind. We do not have good enough UV phase coverage to verify that higher ionization UV lines such as C IV or N V are also produced in the ionized wind.

Detailed illumination models generally account for the observed fluxes of the low and moderate ionization emission lines. The H I and He I fluxes imply larger mass loss rates in the red giant wind than the fluxes of other emission lines. Because the H II and He II recombination regions in the red giant atmosphere are difficult to model accurately, Proga et al. (1996, 1998) noted that their illumination models underestimate the fluxes of these lines. The illumination models thus imply a mass loss rate of  $\sim 10^{-7} M_{\odot} \text{ yr}^{-1}$  if the red giant wind has a geometric cross-section of  $\sim 2^2\text{--}3^2 R_g^2$ . This mass loss rate is comparable to mass loss rates derived for the red giants in AG Peg and other symbiotic stars (see Kenny et al. 1991; Seaquist & Taylor 1992; Seaquist, Krogulec, & Taylor 1993; Ivison et al. 1995).

The UV data imply that the hot component continues to decline in luminosity. Figure 7 summarizes the evolution of the optical and bolometric magnitude  $M_{bol}$  of the hot component since its eruption in the mid 1800's. The dashed line indicates the evolution of the optical continuum. The symbols indicate the evolution of  $M_{bol}$ . Data shown as filled symbols without boxes adopt bolometric corrections to estimate  $M_{bol}$  from optical spectra (Kenyon et al. 1993); data shown as filled symbols inside boxes use UV data from this paper and Kenyon et al. (1993). As described by Gallagher et al. (1979) and Kenyon et al. (1993), the hot component maintained a roughly constant  $M_{bol}$  from 1900–1980 and then began to decline. Our new data suggest a factor of 2–3 decline in luminosity and a 10%–20% decline in effective temperature. Further UV observations are necessary to follow the evolution of the hot component to quiescence.

The high ionization forbidden lines indicate that some portion of the nebula is mechanically heated to temperatures of  $10^5$  K or larger. This region has a density of  $\lesssim 10^7 \text{ cm}^{-3}$  and lies at least 10–30 AU from the central binary. If our estimates for the effective temperature and luminosity of

the hot component are correct, the hot component emits enough high energy photons to produce the observed level of emission from high ionization forbidden lines. Shocks in the red giant wind are a potential excitation mechanism for this gas, but the kinetic energy in the winds from the hot component and the red giant is smaller than the emitted energy by a factor of  $\sim 10$  or more. Because it has a very low density, a compressed shell in the inner radio nebula also seems an unlikely source of forbidden line emission in AG Peg. However, this region has an emission measure and gas velocity close to our estimates for the  $\text{Ne}^{+4}$ – $\text{Fe}^{+6}$  zone. Additional high resolution imaging and spectroscopic observations are needed to understand this emission. Detailed photoionization calculations of shocked gas are necessary to see if a combination of photoionization and mechanical heating can explain the large amount of emission from high ionization forbidden lines in this system.

We acknowledge support from an archival grant from the Space Telescope Science Institute, AR-08369-01-A, and from the Smithsonian Astrophysical Observatory. This work was performed while D.P. held a National Research Council Research Associateship at NASA/GSFC. We thank J. Raymond for advice and comments on our analysis of the high ionization forbidden lines.

## REFERENCES

- Arnaud, M., & Raymond, J. 1992, *ApJ*, 398, 394
- Barnes, J. V., & Hayes, D. S. 1982, *IRS Standard Star Manual*, NOAO, Tucson
- Belyakina, T. S. 1968a, *Izv. Krym. Astrofiz. Obs.*, 38, 171
- Belyakina, T. S. 1968b, *Astr. Zh.*, 45, 139
- Belyakina, T. S. 1970, *Astrofizika*, 6, 49
- Boyarchuk, A. A. 1966, *Astr. Zh.*, 43, 976
- Boyarchuk, A. A. 1967, *Astr. Zh.*, 44, 12
- Contini, M. 1997, *ApJ*, 483, 887
- Contini, M., & Formigini, L. 1999, *ApJ*, 517, 925
- Fabricant, D. G., Cheimets, P., Caldwell, N., & Geary, J. 1998, *PASP*, 110, 79
- Ferland, G. J., & Shields, G. A. 1978, *ApJ*, 226, 17
- Fernández-Castro, T., Cassatella, A., Giménez, A., & Viotti, R. 1988, *ApJ*, 324, 1016
- Fernie, J. D. 1985, *PASP*, 97, 653
- Fleming, W. P. 1907. *Ann. Harv. Coll. Obs.*, 47, 1
- Formigini, L., Contini, M., & Leibowitz, E. M. 1995, *MNRAS*, 277, 1071
- Gallagher, J. S., Holm, A. V., Anderson, C. M., & Webbink, R. F. 1979, *ApJ*, 229, 994
- Girard, T., & Willson, L. A. 1987, *A&A*, 183, 247
- Hayes, D., & Latham, D. 1975, *ApJ*, 197, 593
- Hillier, D. J. 1987, *ApJS*, 63, 965
- Iijima, T. 1981, in *Photometric and Spectroscopic Binary Systems*, edited by E. B. Carling & Z. Kopal, Reidel, Dordrecht, p. 517
- Iverson, R. J., Seaquist, E. R., Schwarz, H. E., Hughes, D. H., & Bode, M. F. 1995, *MNRAS*, 273, 517
- Kafatos, M., & Lynch, J. P. 1980, *ApJS*, 42, 611
- Keenan, F. P., & Norrington, P. H. 1987, *A&A*, 181, 370

- Keenan, F. P., & Norrington, P. H. 1991, *ApJ*, 368, 486
- Kenny, H. T., Taylor, A. R., & Seaquist, E. R. 1991, *ApJ*, 366, 549
- Kenyon, S. J. 1985, in *Cataclysmic Variables and Low Mass X-Ray Binaries*, edited by D. Q. Lamb & J. Patterson, Reidel, Dordrecht, p. 417.
- Kenyon, S. J. 1986, *The Symbiotic Stars*, Cambridge University, Cambridge
- Kenyon, S. J., & Fernández-Castro, T. 1987, *AJ*, 93, 938
- Kenyon, S. J., & Gallagher, J. S. 1983, *AJ*, 88, 666
- Kenyon, S. J., Mikołajewska, J., Mikołajewski, M., Polidan, R. S., & Slovak, M. H. 1993, *AJ*, 105, 1573
- Kenyon, S. J., Oliverson, N. G., Mikołajewska, J., Mikołajewski, M., Garcia, M. R., Stencel, R. E., & Anderson, C. M. 1991, *AJ*, 101, 637
- Kenyon, S. J., & Truran, J. W. 1983, *ApJ*, 273, 280
- Kenyon, S. J., & Webbink, R. F. 1984, *ApJ*, 279, 252
- Keyes, C. D. 1981, Ph. D. thesis, Univ of California, Los Angeles
- Keyes, C. D. 1997, *Hubble Space Telescope Data Handbook, Version 3, Volume II*, Space Telescope Science Institute
- Kwok, S., & Leahy, D. A. 1984, *ApJ*, 283, 675
- Lundmark, K. 1921, *Astr. Nachr.*, 213, 93
- Mathis, J. S. 1990, *ARA&A*, 28, 37
- Merrill, P. W. 1916, *Pub. Michigan Obs.*, 2, 71
- Merrill, P. W. 1929a, *PASP*, 41, 255
- Merrill, P. W. 1929b, *ApJ* 69, 330
- Merrill, P. W. 1959, *ApJ*, 129, 44
- Mürset, U., Jordan, S., & Walder 1995, *A&A*, 297, 87
- Mürset, U., & Nussbaumer, H. 1994, *A&A*, 282, 586
- Mürset, U., Nussbaumer, H., Schmid, H. M., & Vogel, M. 1991, *A&A*, 248, 458
- Mürset, U., & Schmid, H. M. 1999, *A&AS*, 137, 473

- Nussbaumer, H. 1992, in *Evolutionary Processes in Interacting Binary Stars*, IAU Symposium, No. 151, edited by Y. Kondo, R. F. Sisteró, & R. S. Polidan, Kluwer, Dordrecht, p. 429
- Nussbaumer, H., & Rusca, C. 1979, *A&A*, 72, 129
- Nussbaumer, H., Schmutz, W., & Vogel, M. 1995, *A&A*, 293, 13
- Nussbaumer, H., & Storey, P. J. 1982, *A&A*, 115, 205
- Nussbaumer, H., & Vogel, M. 1989, *A&A*, 213, 137
- Nussbaumer, H., & Walder, R. 1993, *A&A*, 278, 209
- Payne-Gaposchkin, C. 1957, *The Galactic Novae*, Amsterdam, North Holland
- Proga, D., Mikołajewskaa, J., & Kenyon, S. J. 1994, *MNRAS*, 268, 213
- Proga, D., Kenyon, S. J., Raymond, J., & Mikołajewska, J. 1996, *ApJ*, 471, 930
- Proga, D., Kenyon, S. J., & Raymond, J. 1998, *ApJ*, 501, 339
- Saraph, H. E., & Seaton, M. J. 1980, *MNRAS*, 193, 617
- Schwank, M., Schmutz, W., & Nussbaumer, H. 1997, *A&A*, 319, 168
- Seaquist, E. R., Krogulec, M., & Taylor, A. R. 1993, *ApJ*, 410, 260
- Seaquist, E. R., & Taylor, A. R. 1992, *ApJ*, 387, 624
- Taylor, A. R., & Seaquist, E. R. 1984, *ApJ*, 286, 263
- Vogel, M. 1991, *A&A*, 249, 173
- Vogel, M., & Nussbaumer, H. 1994, *A&A*, 284, 145
- Wallerstein, G., & Brugel, E. 1988, *A&A*, 197, 182
- Wallerstein, G., Willson, L. A., Salzer, J., & Brugel, E. 1984, *A&A*, 133, 137
- Willson, L. A., Wallerstein, G., Brugel, E. W., & Stencel, R. E. 1984, *A&A*, 133, 154
- Woods, D. T., Shull, J. M., & Sarazin, C. 1981, *ApJ*, 249, 399

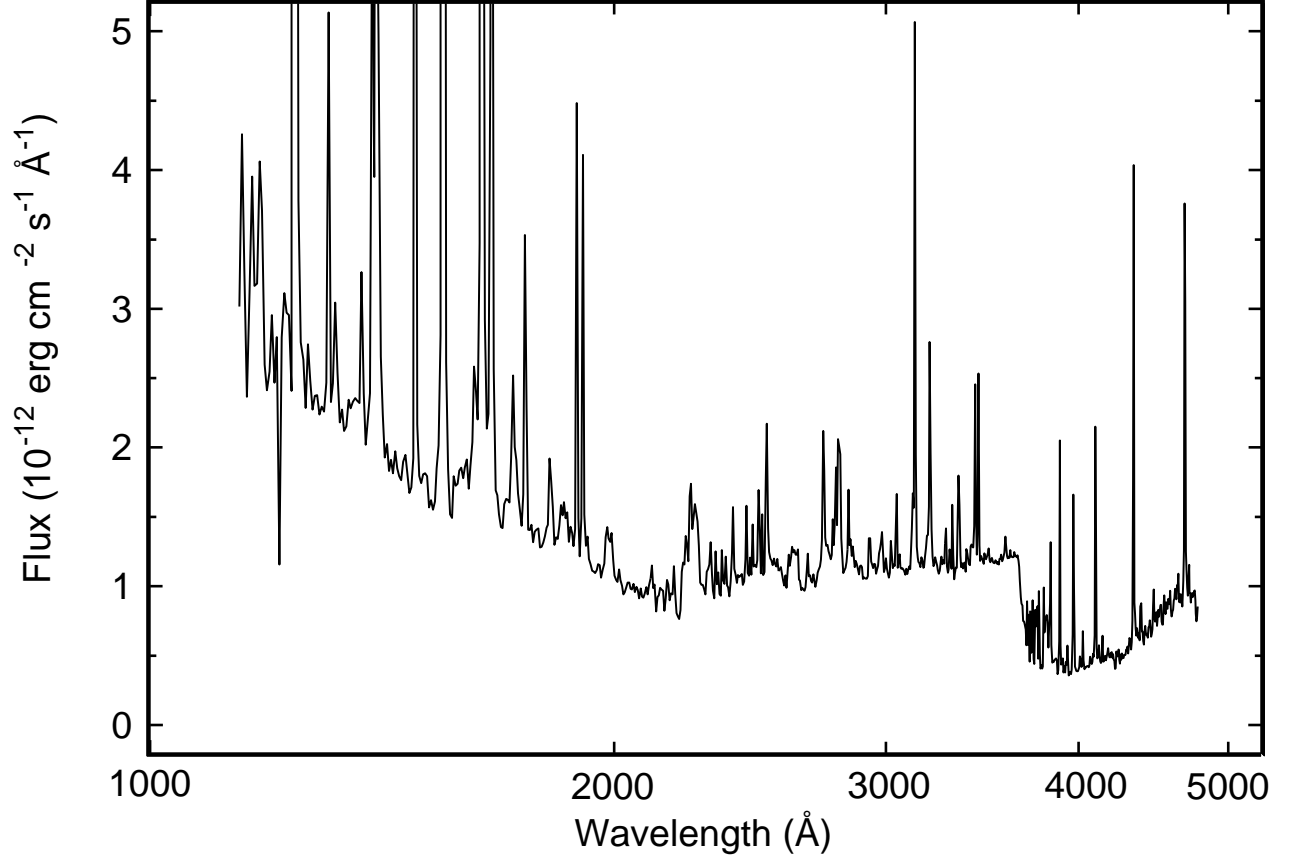


Fig. 1.— *HST* spectrum of AG Peg. The data have not been corrected for interstellar reddening. The continuum consists of the Rayleigh-Jeans tail of a hot blackbody for  $\lambda < 2000$  Å. Strong nebular emission for  $2000 \text{ Å} < \lambda < 3646 \text{ Å}$ , and the Wien side of the red giant spectrum for  $\lambda > 4200 \text{ Å}$ . Intense permitted and forbidden emission lines are visible at all wavelengths.

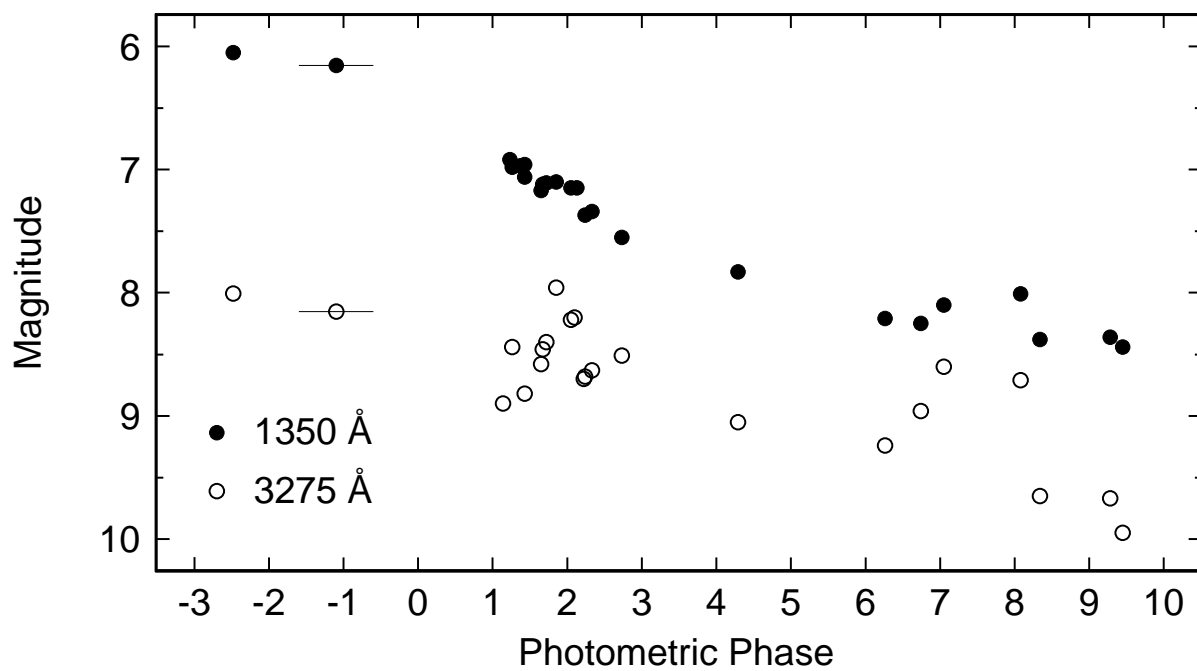


Fig. 2.— Variation of the UV continuum with photometric phase. Except for small rises at integral photometric phases, the 1350 Å and the 3275 Å continua decline with time.

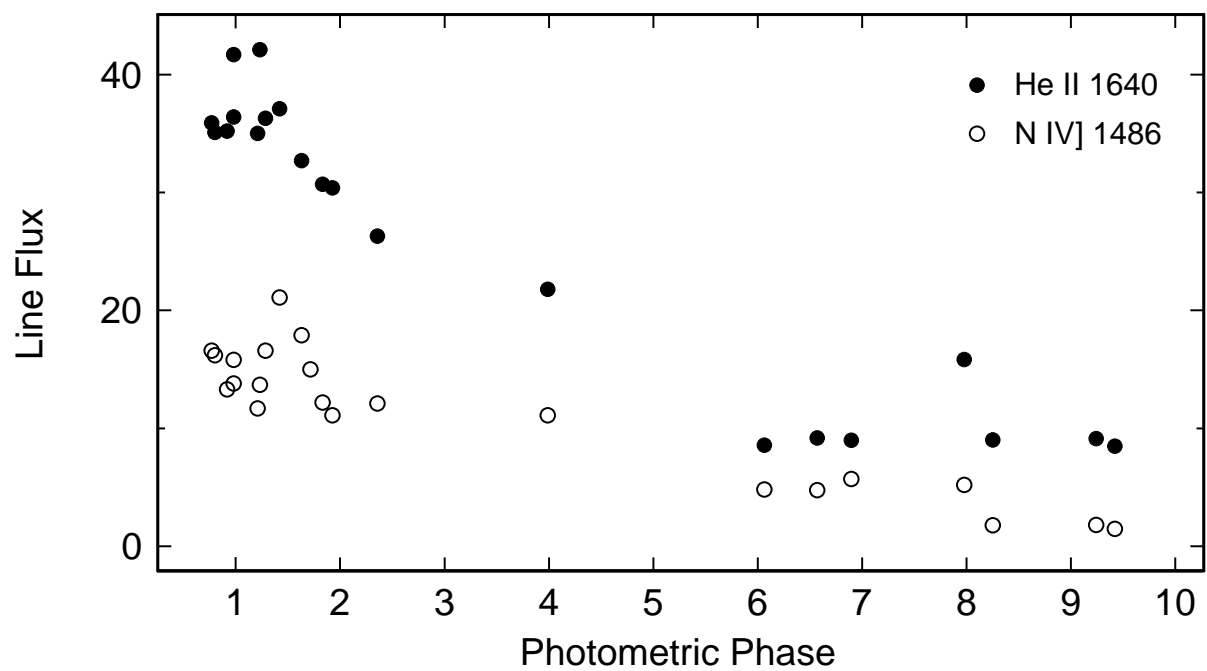


Fig. 3.— Variation of the He II  $\lambda 1640$  and N IV]  $\lambda 1486$  emission lines with photometric phase.

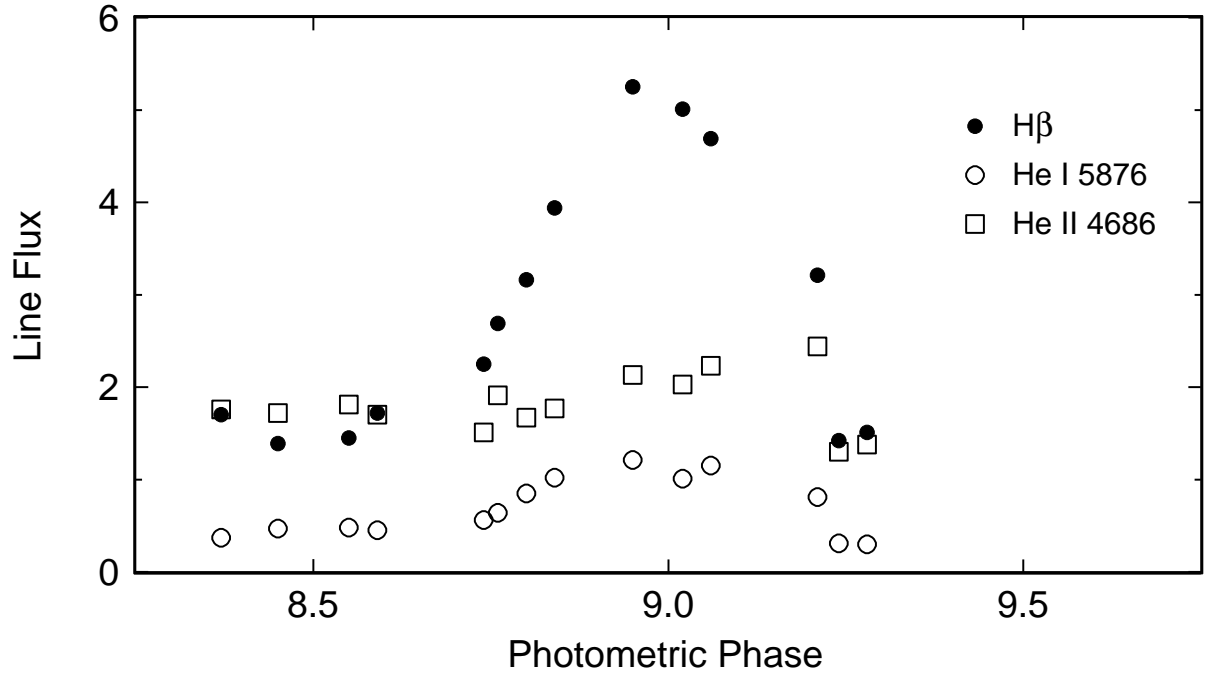


Fig. 4.— Variation of several optical emission lines with photometric phase. All of the H I and He I lines rise by factors of 2–3 at  $\phi = 9$ ; the He II lines increase by less than 50% at  $\phi = 9$ .

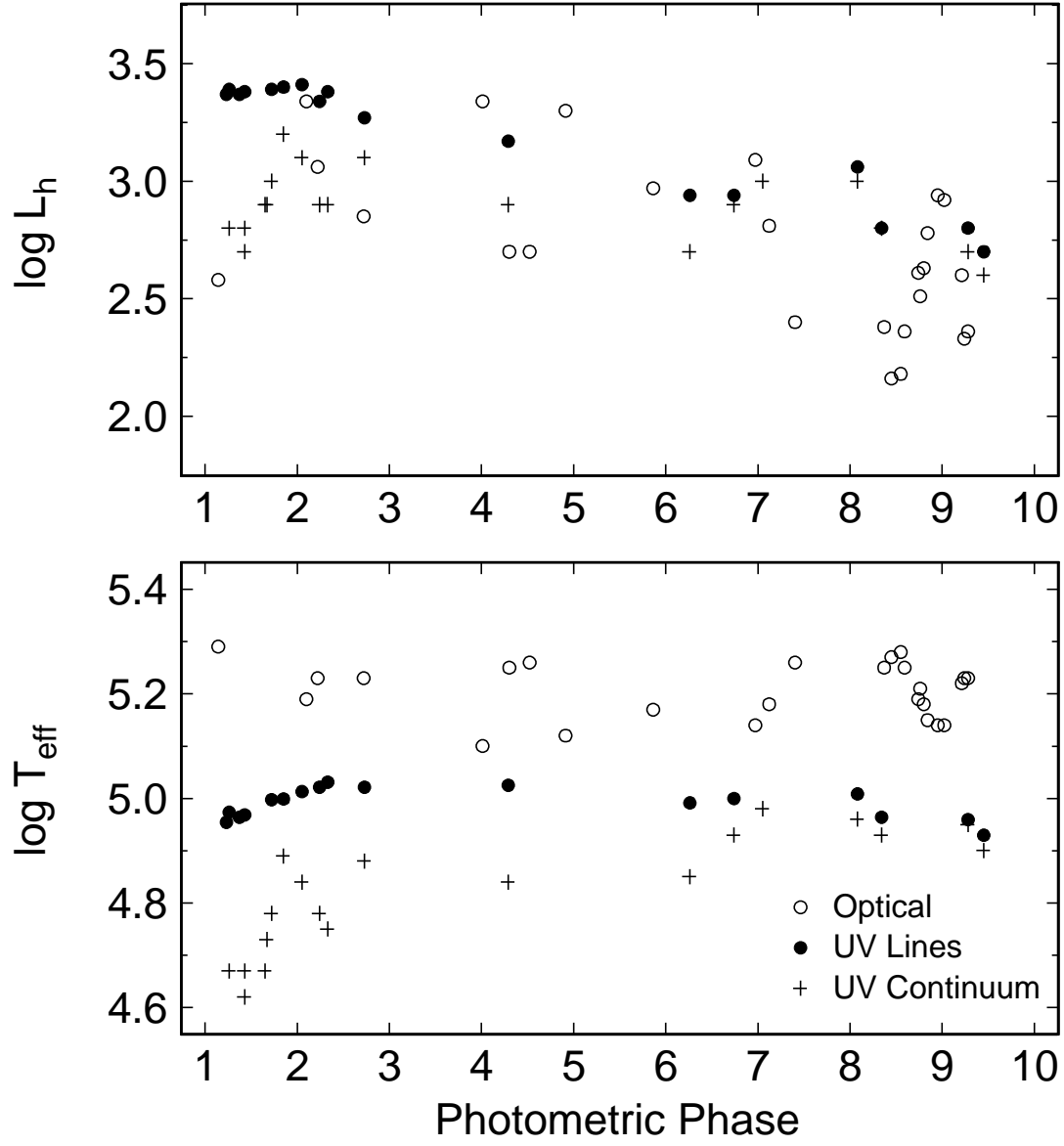


Fig. 5.— Variation of derived luminosity (top panel) and effective temperature (bottom panel) of the hot component as a function of photometric phase.

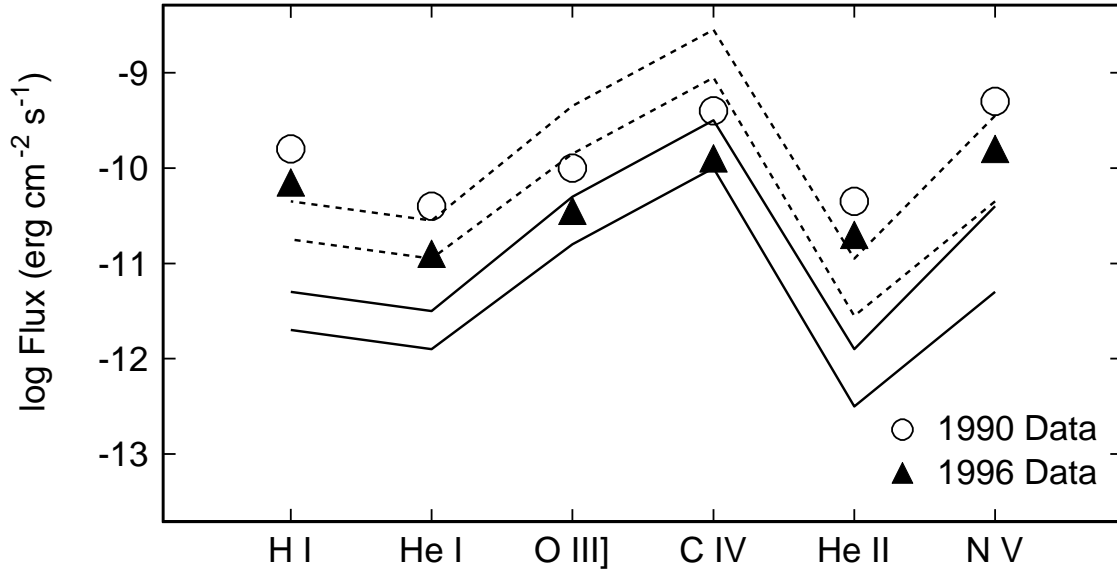


Fig. 6.— Comparison of illumination models with observations of AG Peg. The legend indicates the two epochs of the observations. The models assume Vogel’s velocity law for a wind with  $\log \beta = -2$ , a cross-section of  $R_g^2$  (solid curves) or  $3^2 R_g^2$  (dashed curves), and  $\dot{M} = 10^{-6} M_\odot \text{ yr}^{-1}$  (upper curve) or  $\dot{M} = 10^{-8} M_\odot \text{ yr}^{-1}$  (lower curve). The hot component has an effective temperature of  $10^5$  K.

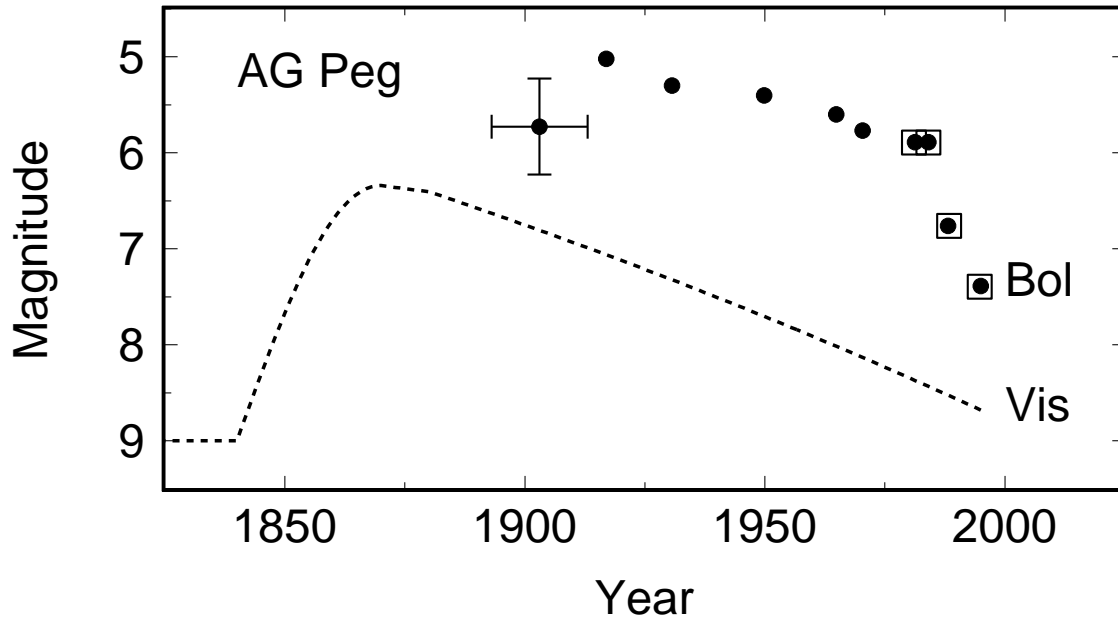


Fig. 7.— Variation of optical (dashed line) and bolometric luminosity (symbols) of the hot component with time. The open circles are luminosities from Kenyon et al. (1993) using bolometric corrections estimated from optical spectra. The cross indicates a typical error bar for these estimates. The open boxes surrounding filled circles are luminosities derived from UV data in this paper and Kenyon et al. (1993).

Table 1. UV Continuum Magnitudes from HST Data

JD	Phase	m <sub>1300</sub>	m <sub>1350</sub>	m <sub>1700</sub>	m <sub>2225</sub>	m <sub>2700</sub>	m <sub>3275</sub>
2449304	8.07	7.95 ± 0.02	8.01 ± 0.02	8.36 ± 0.02	8.63 ± 0.03	8.89 ± 0.03	8.71 ± 0.02
2449516	8.33	8.37 ± 0.03	8.38 ± 0.03	8.77 ± 0.03	9.05 ± 0.04	9.75 ± 0.04	9.65 ± 0.04
2450293	9.27	8.35 ± 0.03	8.36 ± 0.03	8.80 ± 0.03	9.09 ± 0.04	9.77 ± 0.04	9.67 ± 0.04
2450429	9.44	8.44 ± 0.03	8.44 ± 0.03	8.87 ± 0.03	9.15 ± 0.04	9.99 ± 0.04	9.95 ± 0.04

Note. — Phases are computed according to Eq. (2).

Table 2. Optical Continuum Magnitudes

JD	Phase	m <sub>4400</sub>	m <sub>5550</sub>	m <sub>6125</sub>	m <sub>7025</sub>
2448755	7.39	9.51±0.15	8.67±0.03	8.39±0.04	...
2449542	8.36	9.47±0.07	8.58±0.06	8.29±0.05	7.78 ± 0.05
2449609	8.44	9.44±0.07	8.61±0.06	8.35±0.05	7.79 ± 0.05
2449694	8.54	9.44±0.07	8.44±0.06	8.30±0.05	7.81 ± 0.05
2449726	8.58	9.38±0.07	8.45±0.06	8.21±0.05	7.86 ± 0.05
2449844	8.73	9.31±0.07	8.41±0.06	8.25±0.05	7.82 ± 0.05
2449862	8.75	9.40±0.07	8.50±0.06	8.24±0.05	7.84 ± 0.05
2449892	8.79	9.45±0.07	8.50±0.06	8.21±0.05	7.81 ± 0.05
2449926	8.83	9.15±0.07	8.57±0.06	8.13±0.05	7.78 ± 0.05
2450019	8.94	9.06±0.07	8.40±0.06	8.05±0.05	7.69 ± 0.05
2450078	9.01	9.25±0.07	8.40±0.06	8.13±0.05	7.75 ± 0.05
2450108	9.05	9.44±0.07	8.56±0.06	8.27±0.05	7.87 ± 0.05
2450229	9.20	9.40±0.07	8.47±0.06	8.19±0.05	7.77 ± 0.05
2450255	9.23	9.38±0.07	8.50±0.06	8.23±0.05	7.77 ± 0.05
2450284	9.27	9.43±0.07	8.55±0.06	8.25±0.05	7.78 ± 0.05

Note. — Phases are computed according to Eq. (2).

Table 3. HST ultraviolet emission line fluxes

Line ID Photometric Phase	JD - 2400000			
	49304	49516	50293	50429
	8.07	8.33	9.27	9.44
N V 1240	20.51	6.96	6.60	3.48
O I 1305	1.23	0.18	0.27	0.09
O V] 1371	0.66	0.42	0.23	0.20
Si IV 1394	1.49	0.29	0.35	0.13
Si IV,O IV] 1403	5.11	3.52	2.09	1.53
S IV] 1417	0.10	0.04	0.03	0.02
N IV] 1486	5.20	1.78	1.80	1.48
C IV 1550	25.26	6.65	7.01	3.23
[Ne V] 1574	0.12	0.10	0.11	0.12
N V 1619	0.55	0.29	0.22	0.34
He II 1640	15.83	9.03	9.12	8.49
O III] 1664	4.56	1.71	1.63	1.34
N IV 1719	1.29	0.71	0.61	0.41
N III] 1750	1.29	0.61	0.60	0.45
Si III] 1892	1.37	0.42	0.39	0.26
Cl III] 1908	1.20	0.68	0.65	0.53
[Fe VII] 2015	0.05	0.03	0.04	0.03
He II 2306	0.29	0.14	0.13	0.12
C II] 2325	0.16	0.04	0.05	0.04
He II 2385	0.34	0.17	0.16	0.14
He II 2511	0.45	0.49	0.57	0.51
He II 2733	0.50	0.55	0.58	0.56
[Mg V] 2783	0.37	0.30	0.32	0.33
Mg II 2793	0.74	0.19	0.19	0.11
Mg II 2802	0.39	0.11	0.10	0.05
O III 2832	0.18	0.09	0.10	0.09
[Mg V] 2930	0.23	0.08	0.10	0.09
[Ne V] 2976	0.12	0.05	0.05	0.04
N III 2983	0.15	0.05	0.04	0.03
O III 3023	0.12	0.06	0.08	0.05
O III 3047	0.31	0.14	0.16	0.12
O III 3116	0.27	0.14	0.10	0.07
O III 3133	1.87	0.98	0.92	0.71
He II 3203	1.51	0.87	0.92	0.87

Note. — Fluxes are in units of  $10^{-11} \text{ erg cm}^{-2} \text{ s}^{-1}$

Note. — Phases are computed according to Eq. (2).

Table 4. HST optical emission line fluxes

Line ID Photometric Phase	JD - 2400000			
	49304	49516	50293	50429
	8.07	8.33	9.27	9.44
O III 3299	0.05	0.04	0.03	0.03
O III 3341	0.34	0.15	0.09	0.11
[Ne V] 3346	0.10	0.20	0.11	0.22
[Ne V] 3426	0.72	0.64	0.21	0.66
O III 3444	0.64	0.23	0.18	0.18
[Fe VII] 3586	0.12	0.07	0.08	0.07
H I 3750	0.25	0.06	0.05	0.04
[Fe VII] 3758	0.35	0.24	0.21	0.18
H I 3771	0.27	0.08	0.06	0.06
H I 3798	0.28	0.05	0.04	0.04
H I 3835	0.35	0.21	0.19	0.21
H I 3888	0.38	0.20	0.16	0.14
[Fe VI] 3905	0.05	0.04	0.04	0.03
He I 3927	0.08	0.02	0.02	0.02
He I 3965	0.14	0.04	0.02	0.02
H I 3970	0.78	0.21	0.14	0.14
He I 4009	0.06	0.04	0.03	0.02
He I 4026	0.15	0.08	0.07	0.06
H I 4101	1.14	0.44	0.31	0.35
He I 4121	0.05	0.02	0.02	0.02
He I 4144	0.07	0.03	0.03	0.02
H I 4340	2.02	0.63	0.47	0.52
He I 4388	0.17	0.09	0.05	0.06
He I 4471	0.15	0.07	0.05	0.05
He II 4541	0.16	0.11	0.07	0.08
He II 4686	2.17	1.55	1.35	1.29
He I 4713	0.13	0.06	0.06	0.05

Note. — Fluxes are in units of  $10^{-11}$  erg cm $^{-2}$  s $^{-1}$

Note. — Phases are computed according to Eq. (1).

Table 5. Optical emission line fluxes in units of  $10^{-11}$  erg cm $^{-2}$  s $^{-1}$ .

Line ID	Julian Date - 2440000														
	8755	9542	9609	9694	9726	9844	9862	9892	9926	10019	10078	10108	10229	10255	10284
Photometric Phase	7.39	8.36	8.44	8.54	8.58	8.73	8.75	8.79	8.83	8.94	9.01	9.05	9.20	9.23	9.27
[Fe VII] 3586	0.13	...	...	...	...	...	...	...	...	...	...	...	...	...	...
[Fe VII] 3759	0.34	...	...	...	...	...	0.27	...	...	...	...	...	...	...	...
H I 3835	0.35	0.21	...	...	...	...	0.40	0.41	0.46	0.38	0.45	0.56	0.44	0.20	0.19
H I 3888	0.34	0.20	0.16	0.17	0.15	0.33	0.38	0.47	0.51	0.48	0.52	0.78	0.53	0.19	0.20
H I 3970	0.36	0.22	0.21	0.20	0.23	0.34	0.40	0.77	0.81	0.98	0.89	0.85	0.55	0.21	0.21
He I 4009	0.05	0.03	0.06	0.06	0.05	0.03	0.05	0.09	0.07	0.11	0.09	0.07	0.06	0.05	0.03
He II 4026	0.13	0.07	0.09	0.08	0.07	0.05	0.12	0.14	0.15	0.15	0.12	0.10	0.08	0.07	0.06
H I 4101	0.66	0.45	0.40	0.43	0.46	0.51	0.61	0.72	0.90	1.34	1.17	1.09	0.83	0.40	0.36
H I 4340	0.82	0.71	0.74	0.78	0.73	0.91	1.07	1.15	1.41	2.18	1.88	1.69	1.38	0.55	0.59
He I 4388	0.11	0.09	0.07	0.08	0.07	0.08	0.11	0.11	0.13	0.22	0.12	0.22	0.10	0.06	0.05
He I 4471	0.12	0.08	0.07	0.08	0.06	0.08	0.11	0.11	0.13	0.25	0.13	0.15	0.07	0.04	0.05
He II 4541	0.14	0.11	0.08	0.09	0.07	0.08	0.05	0.07	0.06	0.05	0.05	0.07	0.06	0.07	0.08
He II 4686	2.14	1.76	1.72	1.81	1.70	1.51	1.91	1.67	1.77	2.13	2.03	2.23	2.44	1.30	1.38
He I 4713	0.15	0.07	0.06	0.07	0.05	0.06	0.07	0.06	0.08	0.05	0.05	0.06	0.06	0.05	0.06
H I 4861	2.28	1.70	1.39	1.45	1.72	2.25	2.69	3.16	3.94	5.25	5.01	4.69	3.21	1.42	1.51
He I 4922	0.17	0.15	0.11	0.12	0.10	0.18	0.25	0.32	0.37	0.47	0.51	0.29	0.25	0.20	0.15
He I 5015	0.16	0.11	0.13	0.14	0.23	0.23	0.32	0.30	0.38	0.33	0.34	0.31	0.19	0.09	0.09
[Fe VII] 5721	0.15	0.16	0.15	0.16	0.15	0.13	0.20	0.12	0.12	0.21	0.22	0.22	0.22	0.13	0.12
He I 5876	0.36	0.37	0.47	0.48	0.45	0.56	0.64	0.85	1.02	1.21	1.01	1.15	0.81	0.31	0.30
[Fe VII] 6087	0.21	0.20	0.15	0.16	0.15	0.13	0.17	0.14	0.11	0.19	0.18	0.17	0.20	0.20	0.14
H I 6563	...	10.20	8.53	9.17	9.02	11.3	13.00	12.50	15.70	21.50	21.80	22.50	15.40	8.70	9.25
He I 6678	...	0.67	0.64	0.67	0.65	0.68	0.84	0.99	1.20	1.82	1.62	1.84	0.93	0.55	0.60
He I 7065	...	0.51	0.44	0.47	0.43	0.41	0.49	0.51	0.61	1.13	1.20	1.09	0.49	0.44	0.37
He I 7282	...	0.21	0.22	0.23	0.22	0.23	0.28	0.31	0.32	0.37	0.39	0.41	0.25	0.19	0.16